Chapter 5

CFD based Investigation of Condensation of R-744 Inside Converging-Diverging Nozzles

In this chapter, we perform simulations of the phase change process of R-744 inside converging–diverging nozzles. The aim of this work is to get an idea about the time step required for stable computations, validate the solver settings and understand the phase change dynamics. The results are based on two different compressible phase change solvers available in Ansys CFX, namely, the equilibrium phase change solver and the classical nucleation theory based non-equilibrium solver. We simulate flow through three different nozzle cases from literature for which experimental data on pressure distribution is available. We use the thermophysical 85] 100] equation of state from NIST Refprop. The simulation results show significant influence of the inlet conditions, nozzle geometry and fluid properties on the supercooling levels achieved by the vapor phase inside the nozzles. We observe very small supercooling level ($\sim$ 0.5–2 K) for the flow of R-744 inside 97 131], the inlet conditions for which are near to the critical point. A supercooling of around 20 K is observed for the flow of R-744 132], the inlet state for which is far from the critical point. The accuracy of the results from the above mentioned solvers depends on several factors, among which, the accuracy of the real gas property database is the most important. We observe better results based on the Span-Wagner equation of state available in NIST Refprop. We also present guidelines for obtaining converged solutions from these compressible phase change solvers.

5.1 Details of the Computational Domains and Solver Settings

Here we discuss the computational domains, mesh related details and the different solver options used for simulating the test cases considered in the present work. The experimental pressure distribution data for these test cases is available in open literature. A structured, body fitted, 133] with smaller height of mesh elements near the walls. The very first case considered is the flow of R-744 in a 97], the computational domain for which 5.1). A total of 284739 hexahedras are used in the domain. The wall mesh thickness is gradually varied normal to the walls, the non-dimensional wall distance y^+ varies from 8 near the throat region to 4 in the diverging potion under fully developed flow conditions. 5.2

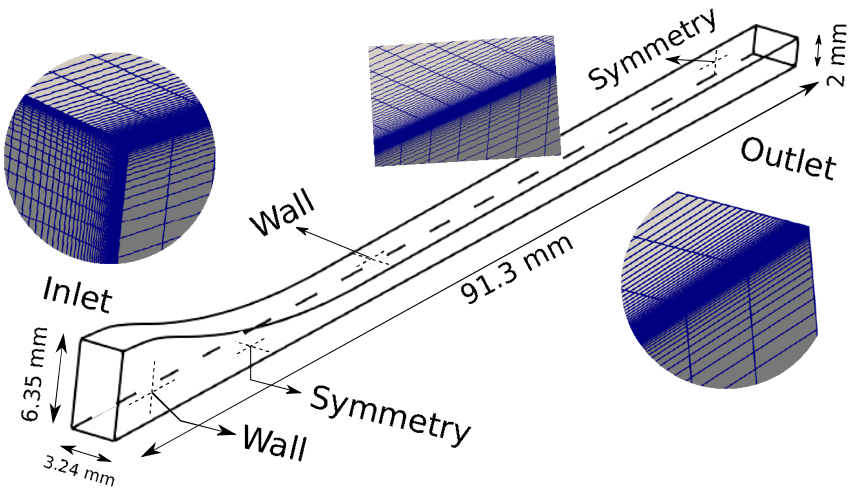

FIGURE 5.1: The computational domain for the flow through a curved converging–diverging 97]. The zoomed views of the structured mesh at the inlet, central and outlet regions are also shown.

96] and Berana et 131]. The mesh for this case has a total of 360477 hexahedras. The non-dimensional wall distance y^+ in this case varies from a maximum of 14 near the throat region to a minimum of 2 in the diverging portion of the nozzle under fully developed flow situation. The last test case is 132] for 5.3). The mesh for this particular case contains a total of 314847 hexahedras. The non-dimensional wall distance y^+ for the mesh is around 6 for this particular test case under fully developed flow condition. The compressible phase change solvers run stably at time steps as low as 10^{-9} second, therefore, the computational requirements are very large. In order to manage the simulations, we are simulating one fourth of the actual physical domains for the Claudio Lettieri and the Berana nozzle cases by using symmetry boundary conditions as shown in the respective figures. For the

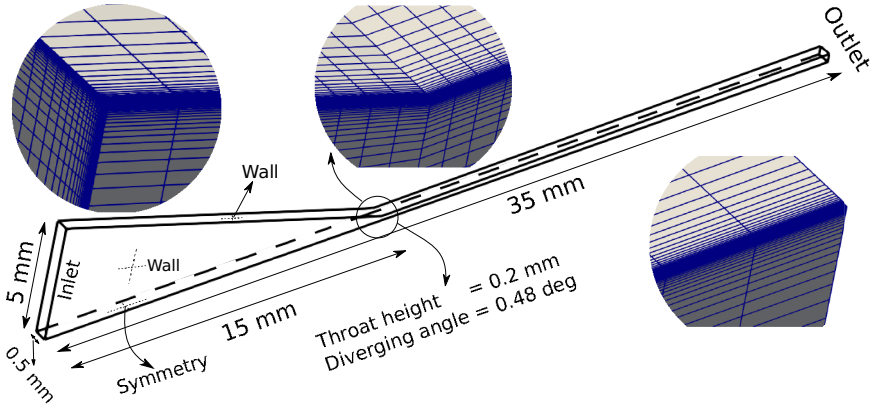

FIGURE 5.2: The computational domain for the flow through a straight converging–diverging 131]. The zoomed views of the structured mesh at the inlet, central and outlet regions are also shown.

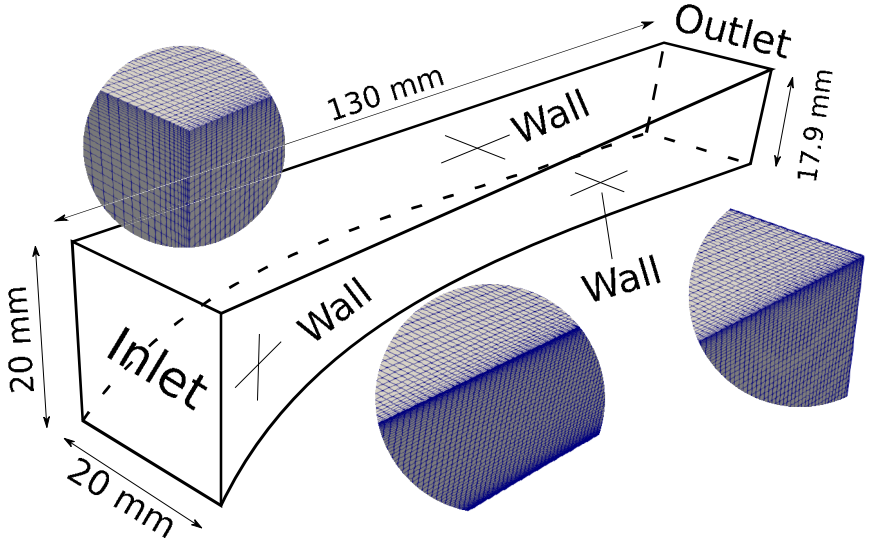

FIGURE 5.3: The computational domain for the flow through a curved converging–diverging 132]. The zoomed views of the structured mesh at the inlet, central and outlet regions are also shown.

case of Gyarmathy nozzle, flow in the full nozzle is simulated. The various boundary conditions 5.1).

The main solver options for the finite volume discretization procedure and for the phase change B.2 B.3 respectively. To obtain a converged solution, the pressure values at the inlet and outlet of the nozzle are respectively increased and decreased as a function of simulation time starting from an average initial condition. This is enabled with the help of CEL B.4 for the Claudio Lettieri test case. The pressure values can similarly be varied as a function of iteration number for the steady B.5. For the non-equilibrium solver, a converged solution could only be attained by adopting the following approach. First, the nucleation process is switched-off in the solver allowing time steps of the order of 10^{-6} second to be used for attaining vapor

TABLE 5.1: Boundary and initial conditions (I.C.) for the various cases

Variable	**Claudio Lettieri**	**Nakagawa**	**Gyarmathy**
Inlet pressure	80 bar	90 bar	40 bar
Outlet pressure	28 bar	35.5 bar	7.4 bar
I.C. pressure	55 bar	65 bar	24 bar
Inlet temperature	311 K	318 K	283 K
I.C. temperature	311 K	318 K	283 K

supercooling in the domain. Afterwards, the nucleation is switched-on allowing phase change to be simulated at time steps of the order of 10^{-9} second. We use the Soave-Redlich-Kwong 134] for the thermophysical properties of R-744, the parameters for which are 5.2). One has to use the expert parameter '`realeos liquid prop = 2`' in Ansys CFX Pre for forcing the solver to read the subcooled liquid properties from real gas equation of state. Better results were obtained with the real gas properties of R-744 obtained from NIST 99 100], the table parameters 5.2 5.2) give a resolution of $\Delta T = 1.16$ K for temperature and $\Delta p = 0.31$ bar for R-744. Similar resolutions 98] for the flow simulation inside supercritical R-744 turbines. Since the flow inside the nozzles is expected to be turbulent, there is a need for a turbulence model to resolve the turbulent momentum fluxes. In the current work, we use the $k-\Omega$ SST model with defaults model parameters for this purpose. A 5% turbulence intensity is assumed at the inlet 95], the critical radius of the droplets is calculated in Ansys CFX based on the Gibbs free energy change of the vapor phase using

$$R_d^* = \frac{2\sigma}{\rho_l \Delta G_v}. \tag{5.1}$$

Near the critical point, the Gibbs free energy change becomes very small due to which the critical radius value become as high as 10^{-3} m in spite of the fact that surface tension also vanishes near the critical point. In order to avoid such nonphysical values, an 'expert parameter' is used in the solver in order to constrain the critical radius to around 10^{-8} m. In the following section, we present the different results obtained by us based on the simulations performed with Ansys CFX.

5.2 Results based on the Soave-Redlich-Kwong equation of state for R-744

In the current section, we discuss the simulation based results obtained using the Soave-Redlich- 134]. First we present the results on the flow of

TABLE 5.2: Real gas property table parameters for the different equations of state used in this work.

Variable	Value
Minimum Temperature	220.0 K
Maximum Temperature	800.0 K
Minimum Pressure	6.0 bar
Maximum Pressure	160.0 bar
No. of points for pressure	500
No. of points for temperature	500

supercritical R-744 through a nozzle, the experiments on which were performed by Lettieri et 97]. We call this test case as the Claudio Lettieri nozzle test case. Next we present the simulation results related to the flow of supercritical R-744 in a converging diverging nozzle with 131]. We call this particular test case as the Berana nozzle test case. Finally, we present the simulation results 132] which we call as the Gyarmathy nozzle test case. These representative test cases have different geometrical shapes, these also involve different inlet states and expansion rates of the working fluids.

5.2.1 Claudio Lettieri nozzle test case

Here we discuss the results related to the flow of R-744 inside the Claudio Lettieri nozzle. To get an idea about the accuracy of the numerical setup, we compare the experimental and simulation 5.4

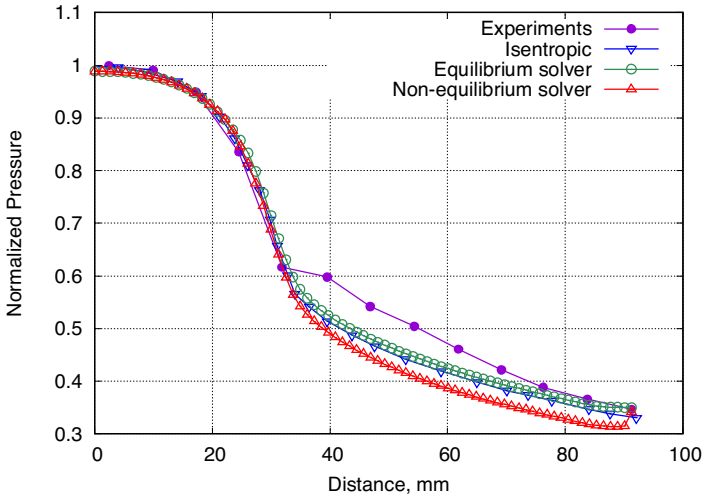

FIGURE 5.4: Variation of the pressure along the Claudio Lettieri nozzle center line based on the 97] and the two compressible phase change solvers in Ansys CFX. The pressure at the inlet to the nozzle (8 MPa) is used for normalization.

distribution along the center line of the Claudio Lettieri nozzle along with those based on the

numerical simulations using the equilibrium and non-equilibrium phase change solvers in Ansys CFX. As can be seen, the equilibrium solver gives a better pressure distribution in the nozzle. This may be due to the more number of model parameters for the non-equilibrium solver which require fine tuning for obtaining accurate results. The non-equilibrium solver under predicts the pressure in the diverging part of the nozzle which can be attributed to the solver parameters such as the maximum critical radius, bulk nucleation tension factor, interphase transfer model

5.5) shows the distribution of the pressure and vapor temperature inside the Claudio Lettieri nozzle based on the non-equilibrium solver. The fluid cools down as it expands inside the nozzle with a minimum temperature equal to 265 K at the exit of the nozzle. A similar

5.6) compares the liquid

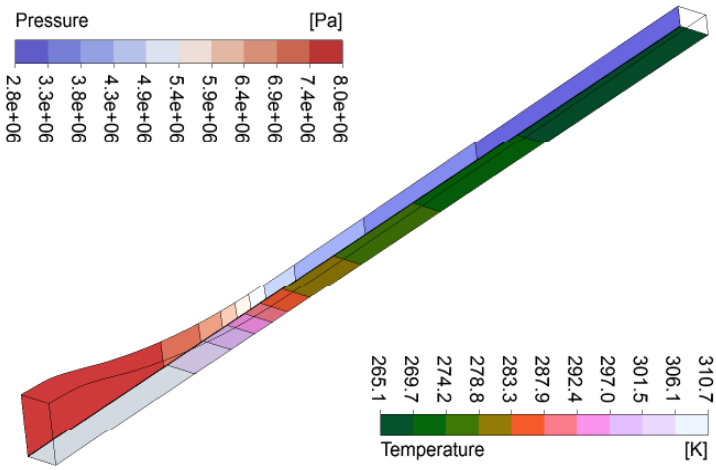

FIGURE 5.5: Distribution of the absolute pressure and the vapor temperature inside the Claudio Lettieri nozzle calculated based on the non-equilibrium solver.

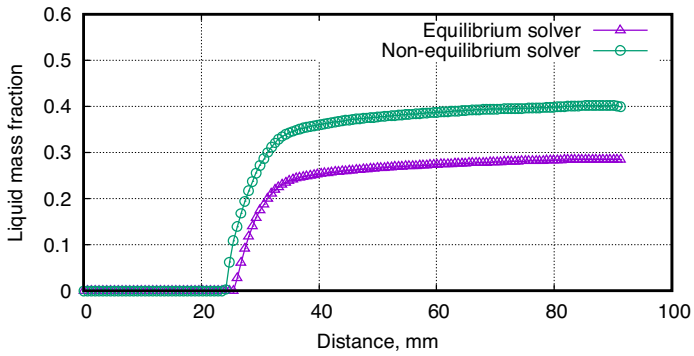

FIGURE 5.6: Comparison of the liquid mass fraction distribution along the Claudio Lettieri nozzle center line based on the equilibrium and the non-equilibrium solvers.

mass fraction distribution inside the Claudio Lettieri nozzle based on the the equilibrium and the non-equilibrium solvers. It can be seen that the maximum liquid mass fraction at the nozzle outlet is around 0.3 based on the equilibrium solver while it is equal to 0.4 with the non-equilibrium solver.

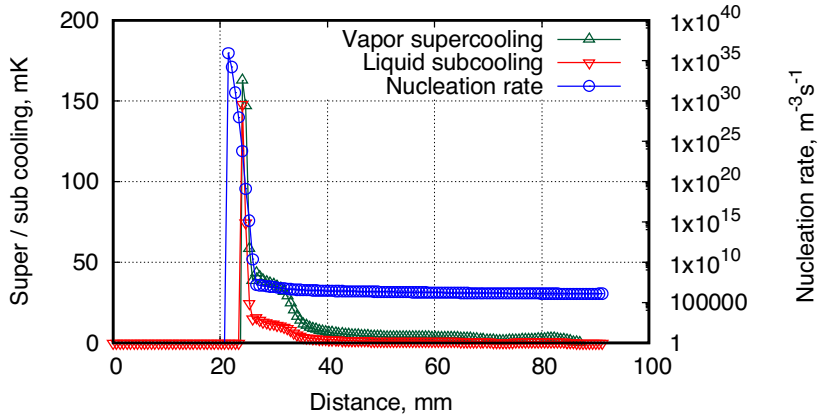

FIGURE 5.7: Distribution of the liquid subcooling, vapor supercooling and the nucleation rate along the Claudio Lettieri nozzle center line calculated based on the non-equilibrium solver.

The non-equilibrium solver gives information on several other parameters which are discussed 5.7) shows the distribution of the vapor supercooling level, the liquid subcooling level and the nucleation rate along the Claudio Lettieri nozzle center line. It can be noted that there are very small (~ 0.15 K) supercooling / subcooling levels achieved by the vapor and the liquid phases of R-744 while expanding through the nozzle. The figure also shows that there is a very high droplet nucleation intensity ($\sim 10^{35}$ nucleation per m^3 per second) confined to a narrow portion of the nozzle length near the throat which falls steeply to a much smaller, almost constant value ($\sim 10^7$ nucleation's per m^3 per second) along the downstream of 5.8) represent the same information on two mutually perpendicular, symmetry planes of the nozzle. It can be observed in the figure that the nucleation rate is zero in the converging portion of the nozzle which abruptly becomes very high when the vapor becomes supercooled.

5.9 5.10) show the distribution of the droplet diameter and the droplet number per unit volume inside the Claudio Lettieri nozzle. It can be seen that the droplet size is the smallest near the nucleation zone which then increases steeply to around 65 nanometer in a very short axial distance. Similarly, starting from a negligible value at around 20 mm, the number density of the droplets increases steeply in a very small axial distance, and afterwards, decreases 5.11) shows the distribution of the Mach number and the local speed of sound for the vapor phase of R-744 in the Claudio Lettieri nozzle. It can be seen that flow becomes supersonic in the diverging portion of the nozzle while it is subsonic near the throat of the nozzle. This is in spite of the fact that the local speed of sound is lowest in the throat region implying the flow velocity must also be small in that region. This probably explains the low values of supercooling / subcooling (~ 0.5 K) achieved by the vapor, and hence, low overall non-equilibrium conditions existing in the nozzle.

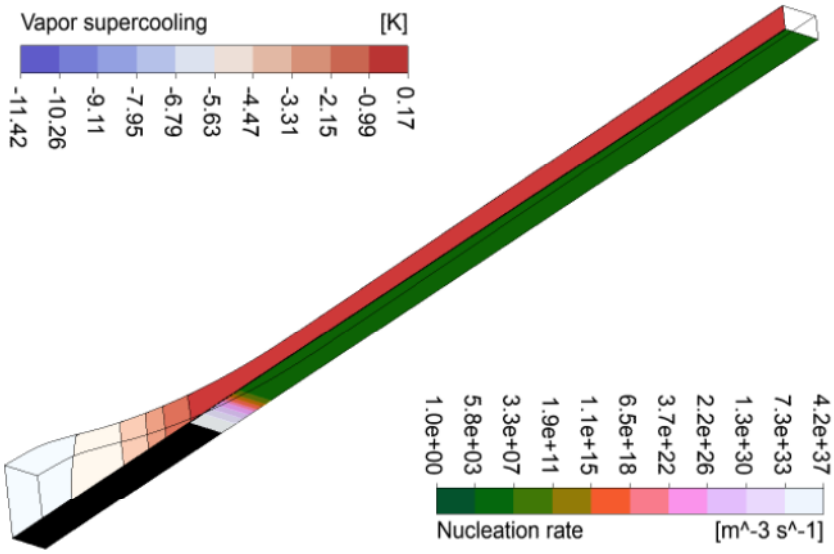

FIGURE 5.8: Contours of the vapor supercooling and the nucleation rate inside the Claudio Lettieri nozzle calculated based on the non-equilibrium solver. The nucleation rate is zero in the converging portion of the nozzle and abruptly becomes very high when the vapor becomes supercooled, although the degree of supercooling is very small.

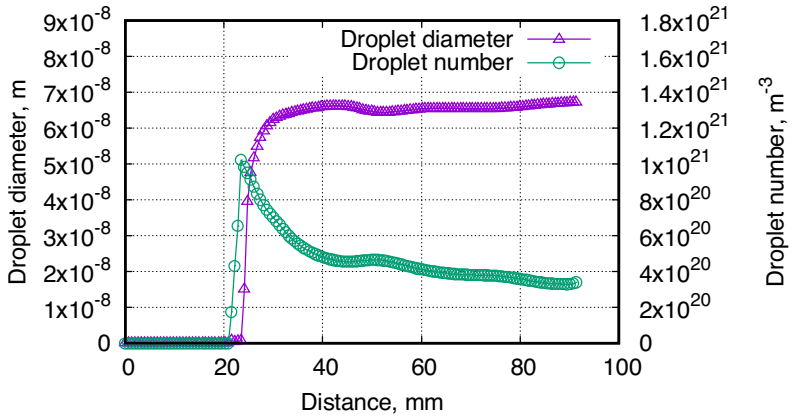

FIGURE 5.9: Distribution of the droplet diameter and droplet number density along the Claudio Lettieri nozzle center line calculated based on the non-equilibrium solver.

5.2.2 Berana nozzle test case

Here we briefly discuss the results on the compressible phase change process of R-744 inside the

131 5.12)

compares the simulation based pressure distribution in the Berana nozzle with the experimentally obtained values. It can be noticed that the equilibrium solver again predicts a more accurate pressure distribution compared to that obtained with the non-equilibrium solver in spite of the better theoretical formulation of the latter. The equilibrium solver predicts a shock wave located immediately downstream to the throat as shown by the kink in the pressure distribution curve. Both the equilibrium and the non-equilibrium solvers under predict the pressure values after the throat of the nozzle. It may be noted here that no experimental data is available for

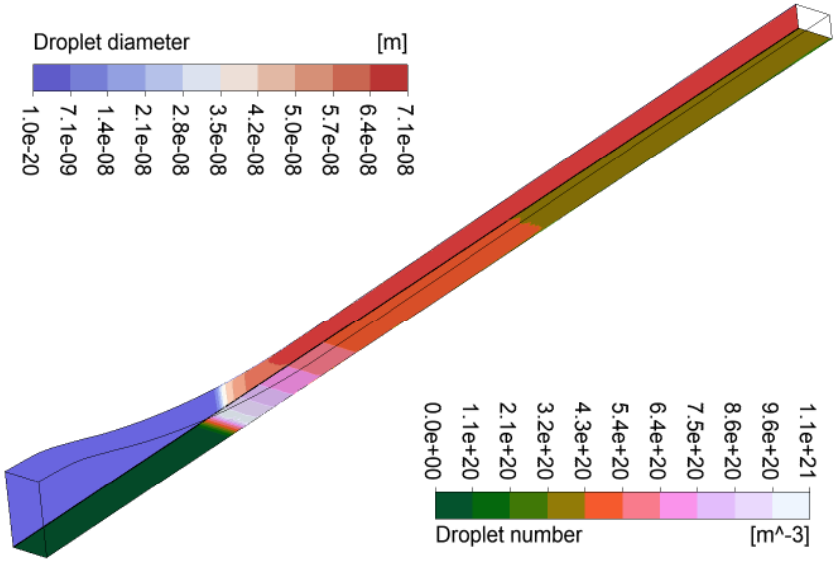

FIGURE 5.10: Contours of the droplet diameter and droplet number inside the Claudio Lettieri nozzle calculated based on the non-equilibrium solver.

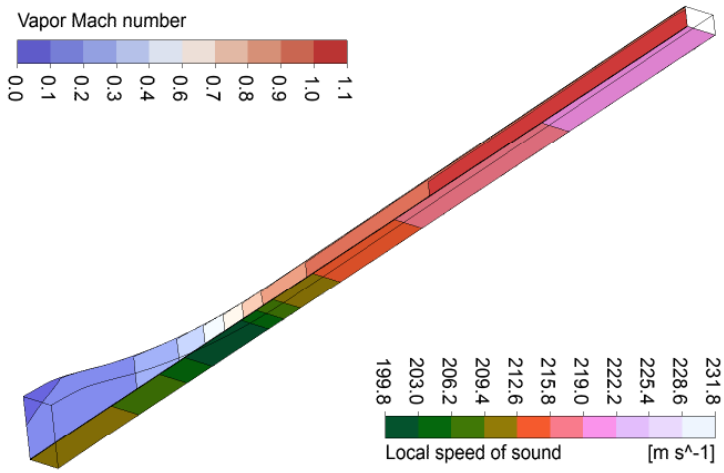

FIGURE 5.11: Distribution of the vapor Mach number and local speed of sound inside the Claudio Lettieri nozzle calculated based on the non-equilibrium solver.

5.13) shows the corresponding pressure contours along with the distribution of vapor temperature in the Berana nozzle. It should be noted that the vapor temperature increases as the throat is approached starting from a value of 318.15 K as the inlet boundary temperature. After the throat, the temperature decreases along the diverging portion of the nozzle.

95] simulated flow inside a two dimensional geometry of the Berana nozzle and observed that the flow becomes supersonic inside the converging portion of the nozzle, that is, before the throat of the nozzle. This is not the case 5.14) where a Mach number of around 0.65 exists at the throat. Information on the distribution of the liquid mass

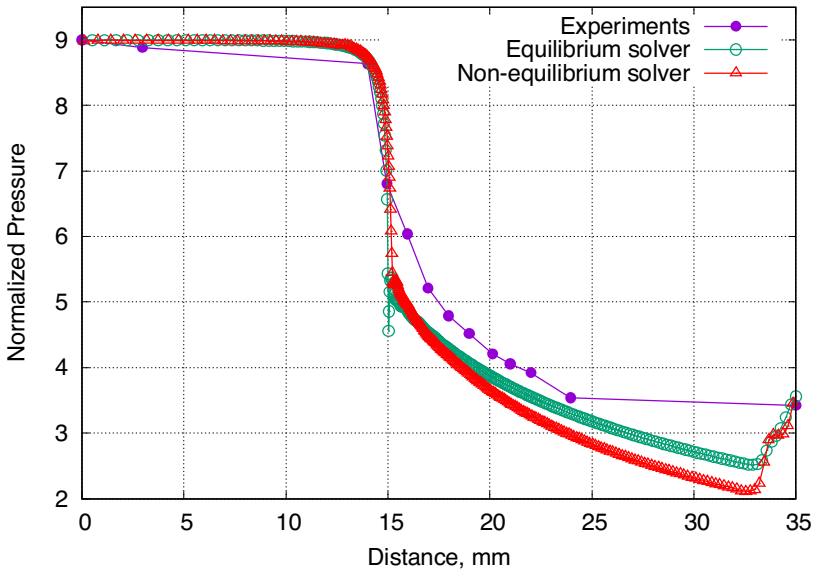

FIGURE 5.12: Variation of pressure along the Berana nozzle center line based on the experiments 131

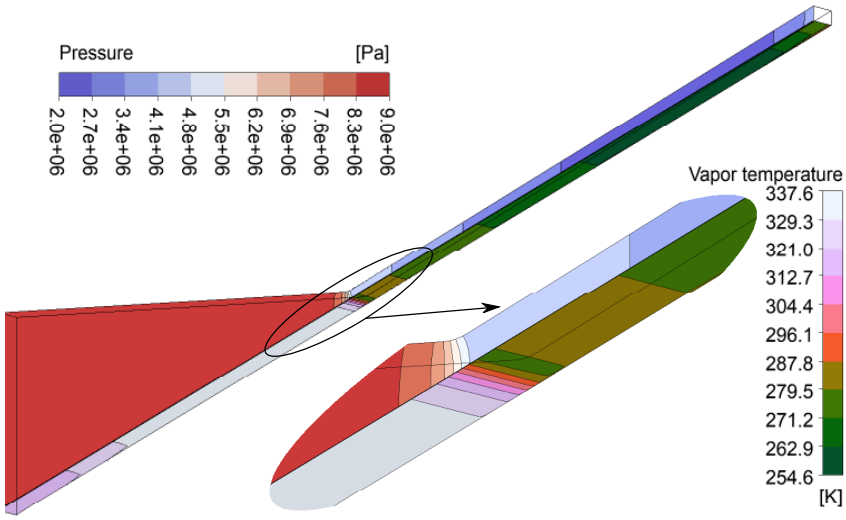

FIGURE 5.13: Distribution of pressure and vapor temperature inside the Berana nozzle based on the non-equilibrium solver. The inlet temperature is equal to 318.15 K. The temperature first increases in the converging part of the nozzle and then decreases after the throat.

5.15). The figure shows that the equilibrium solver predicts a higher value (~ 0.2) of maximum liquid mass fraction distribution inside the nozzle compared to the non-equilibrium solver which gives a maximum value of around 0.16.

5.16) shows the variation of supercooling / subcooling levels achieved by the phases of R-744 and the nucleation rate of the droplets along the center line of the Nakagawa nozzle. In contrast to the Claudio Lettieri nozzle case, the supercooling level here is around 3 K which shows that non-equilibrium effects are stronger in this case. The nucleation rate starts abruptly

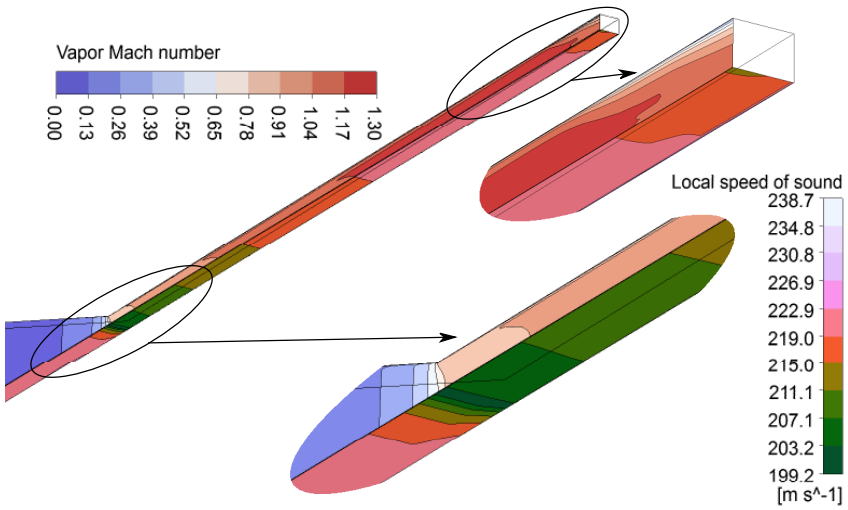

FIGURE 5.14: Contours of the local speed of sound and the Mach number inside the Berana nozzle based on the non-equilibrium solver.

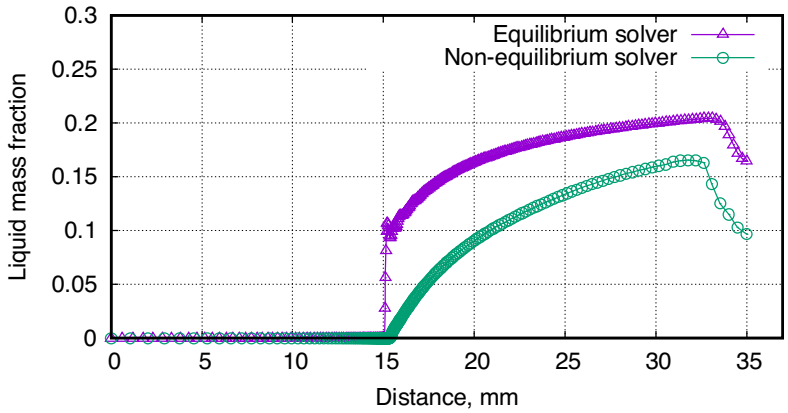

FIGURE 5.15: Comparison of the liquid mass fraction distribution inside the Nakagawa nozzle based on the equilibrium and the non-equilibrium solvers.

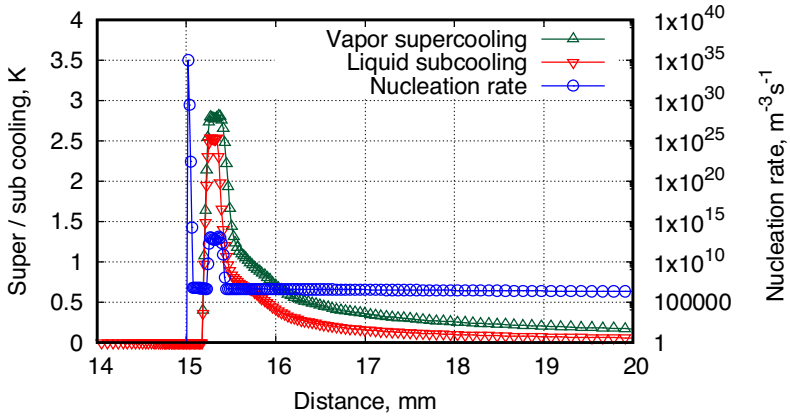

FIGURE 5.16: Distribution of the vapor supercooling and the nucleation rate along the Nakagawa nozzle center line calculated based on the non-equilibrium solver.

with a very high value and then falls steeply as in the Claudio Lettieri case but now undergoes a brief increase before becoming almost constant further downstream the nozzle length. This brief

increase may be due to the higher supercooling / subcooling of the vapor and the liquid phases in that region of the nozzle.

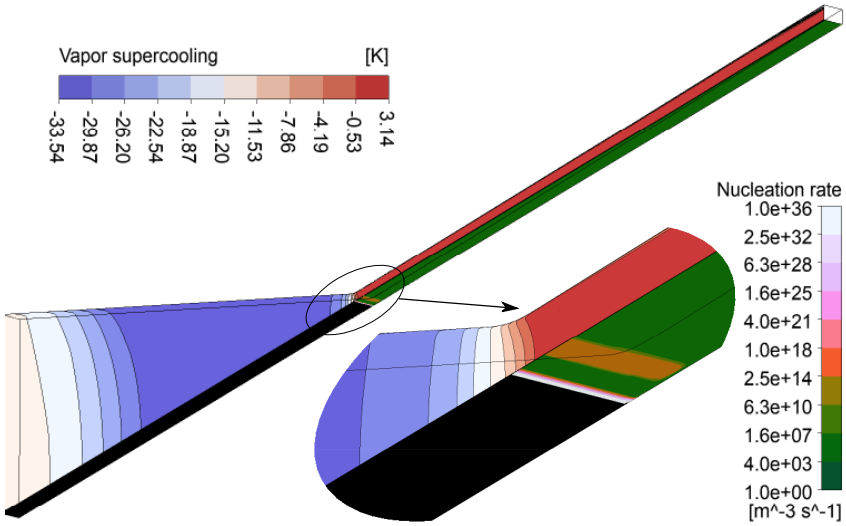

FIGURE 5.17: Distribution of the vapor supercooling and the nucleation rate inside the Nakagawa nozzle based on the non-equilibrium droplets based solver.

5.17) shows the contours of the vapor supercooling and nucleation rate in the Nakagawa nozzle. It should be noted here that the Nakagawa nozzle achieves higher values of vapor supercooling and liquid subcooling compared to those achieved by the Claudio Lettieri nozzle in spite of almost similar pressure difference ($\sim$ 50 bar) across the inlet and the outlet boundaries. This highlights the role of nozzle geometry in the Nakagawa case which has a sharp change in the nozzle shape at the throat region.

5.18) shows the variation of drop diameter and their number density along the Nakagawa nozzle center line. As can be seen, the droplet number density starts with a high value at the throat followed by a sharp decrease, a small increase, and afterwards, a gradual decrease along the downstream of the nozzle. The size of the droplets increase gradually along the length of the nozzle starting from very small values at the throat. It may be noted that the droplet diameter decreases while the droplet number density increases near the exit of the nozzle. This may be due to a shock wave existing in the diverging portion of the nozzle just before the exit as can be

5.14). The liquid mass fraction also decreases

5.15).

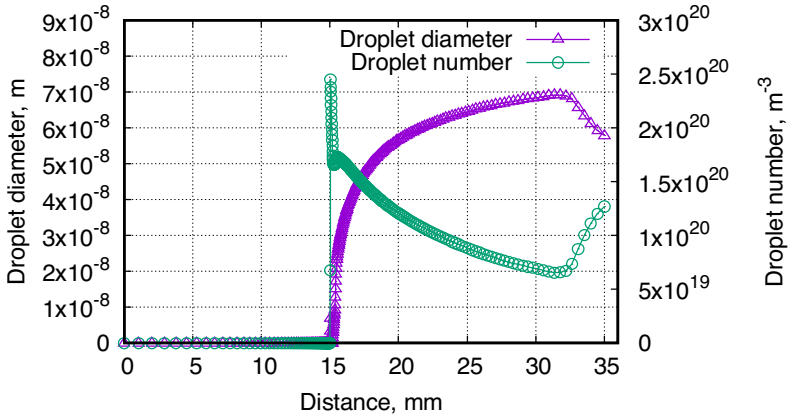

FIGURE 5.18: Distribution of the droplet diameter and their number density along the Nakagawa nozzle center line based on the non-equilibrium solver.

5.3 Results based on the Span-Wagner equation of state for R-744

Here we present the various results related to the flow of R-744 inside three different nozzles with
99]. The equation implemented
100], which
gives more accurate results for R-744 flow inside supercritical turbines and compressors, Ameli et
94 98]. A FORTRAN based code is developed for extracting the thermophysical properties of R-744 from Refprop and the data is written in tabular form for pressure and temperature values falling in the range of 6–160 bar and 220–800 K respectively. Separate data for liquid and vapor phases are written inside .rgp files which can be read by Ansys CFX. As required by the non-equilibrium solver in Ansys CFX, data up to spinodal line for the various properties is extracted using the 'VAPSPNDL' and 'LIQSPNDL' routines in Refprop. We observe that the tabular real gas data from Refprop does not have smooth distribution as a function of different pressure and temperature values. Due to this, the non-equilibrium solver takes very low values of time step ($\sim 10^{-10}$ second) for stable computations. Therefore, we were able to perform only two dimensional simulation for the following test cases.

5.3.1 Claudio Lettieri nozzle

Here we discuss the results on the flow of R-744 through a two dimensional geometry of Claudio
5.19) shows the pressure distribution inside the nozzle based on the
5.20) compares the simulated pressure distribution
along the nozzle center line based on the non-equilibrium solver and Span-Wagner equation of state combination with the experimental pressure data. The simulations again under predict
5.21) shows the simulation based vapor

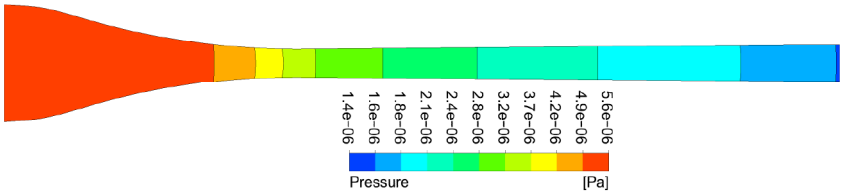

FIGURE 5.19: Pressure distribution inside the Claudio Lettieri nozzle based on the Span-Wagner equation of state.

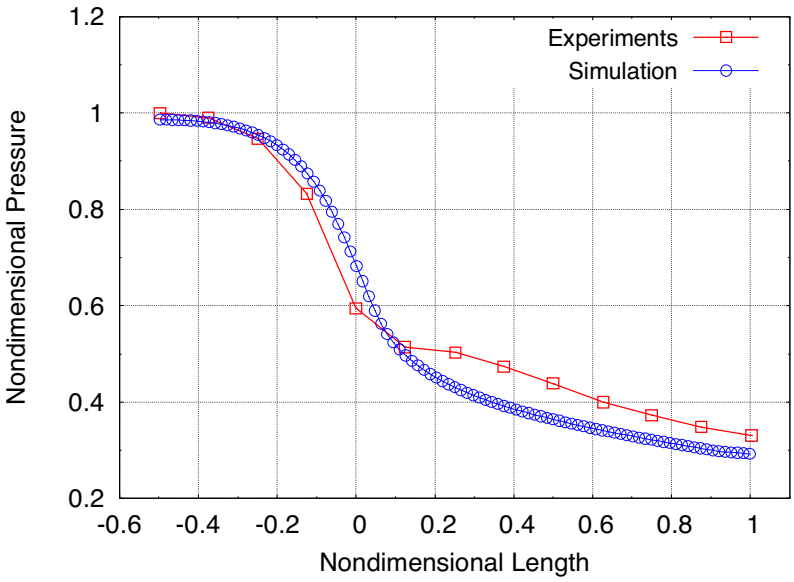

FIGURE 5.20: Comparison of the Claudio Lettieri nozzle center line pressure data based on experiments and simulations with the non-equilibrium solver. The thermophysical properties of R-744 are based on the Span-Wagner equation of state.

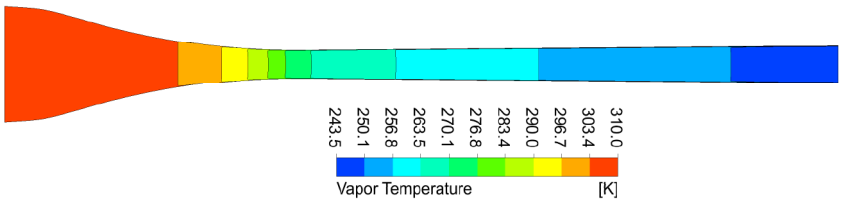

FIGURE 5.21: Vapor temperature distribution inside the Claudio Lettieri nozzle based on the Span-Wagner equation of state.

5.22) shows the Mach number distribution

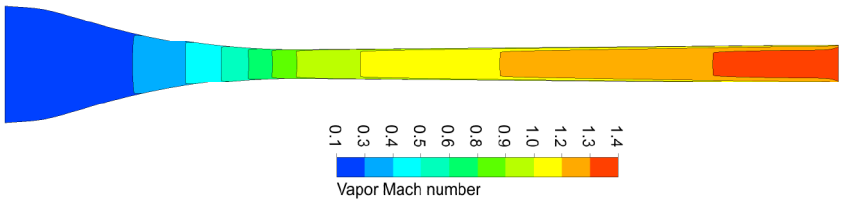

FIGURE 5.22: Mach number distribution inside the Claudio Lettieri nozzle based on the Span-Wagner equation of state.

5.23) shows the local speed of sound distribution inside the nozzle. 5.24) shows the distribution of vapor supercooling inside the nozzle based on the Span-

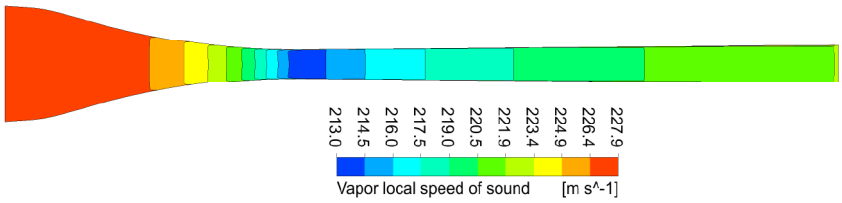

FIGURE 5.23: Local speed of sound (vapor) distribution inside the Claudio Lettieri nozzle based on the Span-Wagner equation of state.

Wagner equation of state. We observe a maximum supercooling of around 1.8 K around the 5.25) shows the surface tension distribution inside the nozzle where the

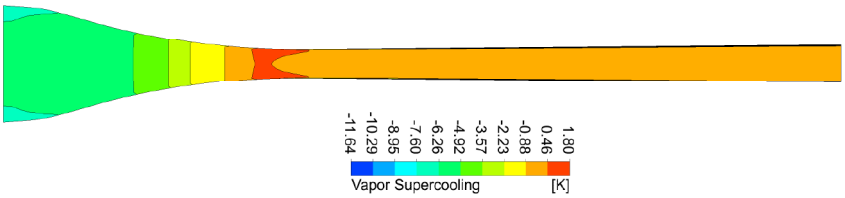

FIGURE 5.24: Vapor supercooling distribution inside the Claudio Lettieri nozzle based on the Span-Wagner equation of state.

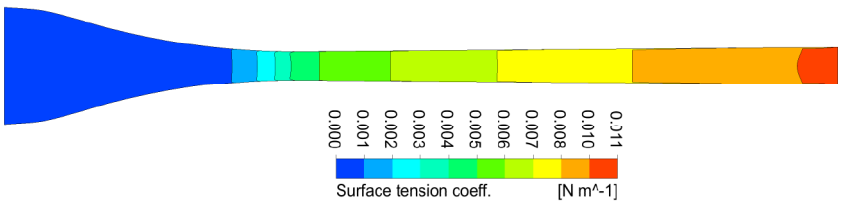

FIGURE 5.25: Surface tension coefficient distribution inside the Claudio Lettieri nozzle based on the Span-Wagner equation of state.

5.26) shows the nucleation rate distribution inside the nozzle. A very high nucleation rate of 10^{31} nucleation per m^3 per second is predicted which abruptly decreases to much lower values, $\sim 10^7$ nucleation per m^3 5.27 5.28

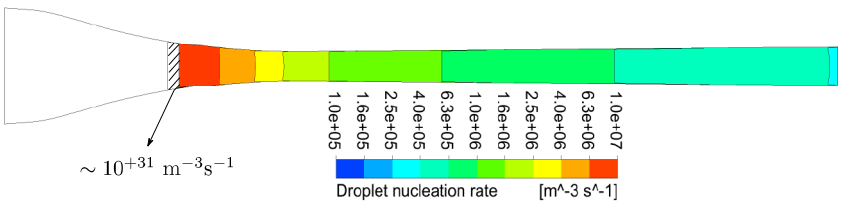

FIGURE 5.26: Nucleation rate distribution inside the Claudio Lettieri nozzle based on the Span-Wagner equation of state.

distribution of droplet number density and the droplet diameter inside the nozzle. As can be

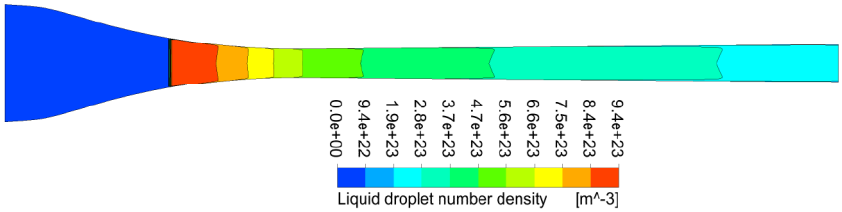

FIGURE 5.27: Droplet number density distribution inside the Claudio Lettieri nozzle based on the Span-Wagner equation of state.

seen, the number density decreases while the droplet diameter increases along the downstream of

5.29) shows the distribution of liquid mass fraction inside the nozzle where

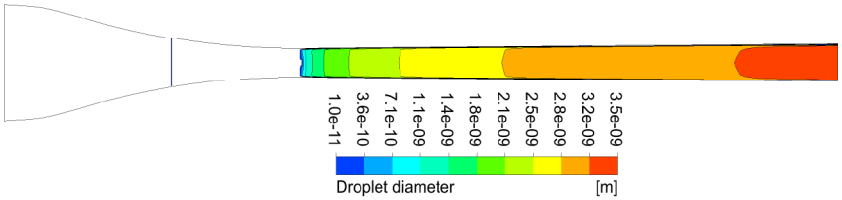

FIGURE 5.28: Droplet diameter distribution inside the Claudio Lettieri nozzle based on the Span-Wagner equation of state.

the maximum amount is less than half of that predicted with the Soave-Redlich-Kwong equation

5.30) shows the mixture entropy distribution inside the nozzle where the

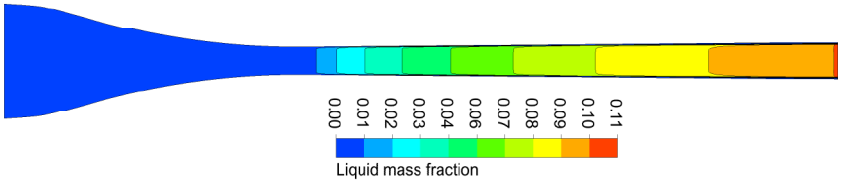

FIGURE 5.29: Liquid mass fraction distribution inside the Claudio Lettieri nozzle based on the Span-Wagner equation of state.

entropy increases along the downstream of the nozzle but there is a small decrease near the throat of the nozzle which is nonphysical since we are using adiabatic boundaries in the nozzle.

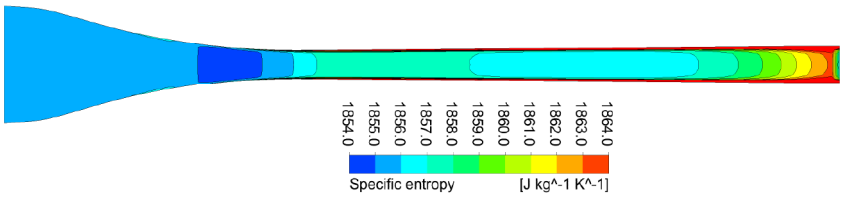

FIGURE 5.30: Fluid entropy distribution inside the Claudio Lettieri nozzle based on the Span-Wagner equation of state.

5.3.2 Berana nozzle

The Berana nozzle test case proved to be very difficult to converge with thermophysical data of R-744 from NIST Refprop which uses the Span-Wagner equation of state. This is in-spite-of using structured, curvilinear, body-fitted meshes. This nozzle has a narrow shape with a sudden change in the geometry at the throat which may be contributing to the non-convergence of results. Another factor is the transcritical operation of the nozzle (inlet pressure equal to 90 bar). The spike in the thermophysical properties like the specific heat at constant pressure, the thermal conductivity at the critical point may also be playing a role here. Since the solver was not converged for this case, we present only the results on the distribution of liquid mass fraction 5.31) shows the distribution of liquid mass fraction inside the

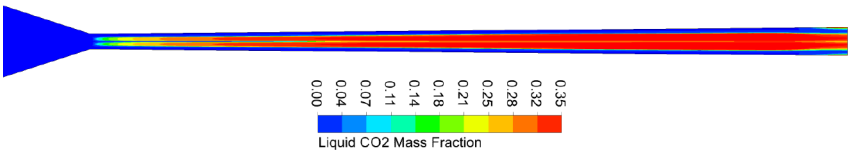

FIGURE 5.31: Liquid mass distribution inside the Berana nozzle based on the Span-Wagner equation of state.

Berana nozzle where the liquid phase is wrongly confined in the central portion of the nozzle. 5.32), there is a very high vapor supercooling ($\sim$ 18 K) in the flow domain near the walls which abruptly reduces to 2 K at locations where the liquid phase exists which is clearly nonphysical.

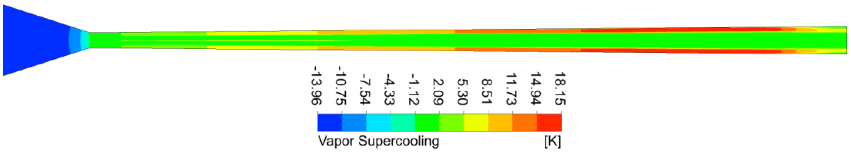

FIGURE 5.32: Vapor supercooling distribution inside the Berana nozzle based on the Span-Wagner equation of state.

5.3.3 Gyarmathy nozzle

Finally, we discuss the results on the condensation of R-744 inside a nozzle originally designed 132]. The nozzle is larger in size and has a higher expansion rate compared to the Claudio Lettieri and the Berana nozzle. The inlet state (40 bar, 283 K) is far from the critical point, one can expect a higher vapor supercooling inside this nozzle. 5.33 5.34) respectively show the distribution of vapor pressure and temperature inside the Gyarmathy nozzle based on the thermophysical properties of R-744 from Span-Wagner equation of state. Compared to the Claudio nozzle, a lower temperature ($\sim$ 220 K) prevails in

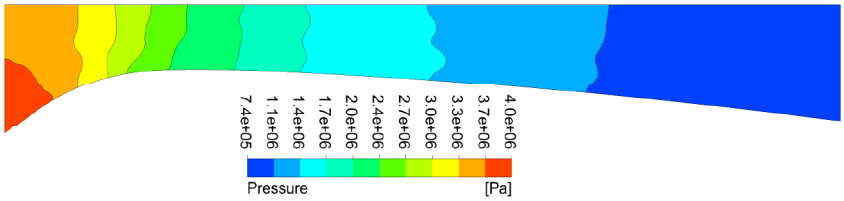

FIGURE 5.33: Pressure distribution inside the Gyarmathy nozzle based on the Span-Wagner equation of state.

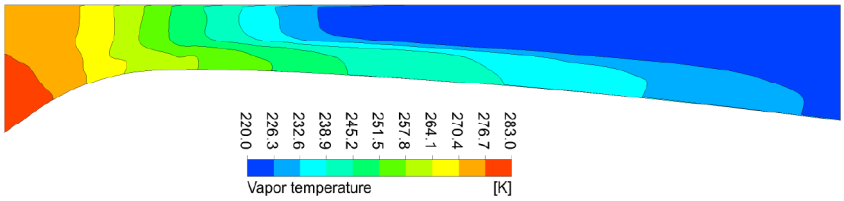

FIGURE 5.34: Vapor temperature distribution inside the Gyarmathy nozzle based on the Span-Wagner equation of state.

5.35), a higher Mach number (~ 1.54) exists at the Gyarmathy nozzle outlet in-spite-of the lower pressure difference across the nozzle.

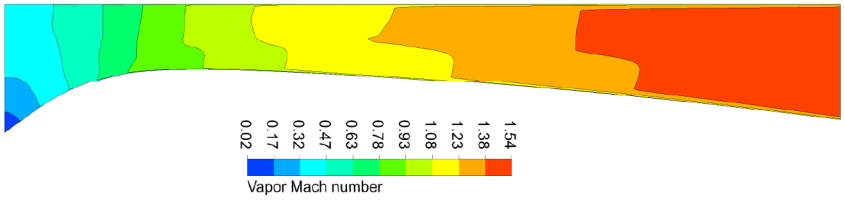

FIGURE 5.35: Mach number distribution inside the Gyarmathy nozzle based on the Span-Wagner equation of state.

5.36) shows the distribution of vapor supercooling inside the Gyarmathy nozzle. As can be observed, the higher flow speed in the nozzle and the fact that the inlet state is away from the critical point causes a higher vapor supercooling (~ 22 K) inside the nozzle. The supercooling is higher at the middle of the nozzle and is confined towards the flat surface of the 5.37) shows the distribution of surface tension coefficient inside the nozzle. It

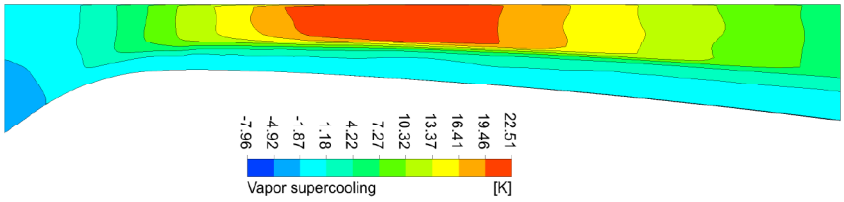

FIGURE 5.36: Vapor supercooling distribution inside the Gyarmathy nozzle based on the Span-Wagner equation of state.

can be noted the surface tension coefficient is higher towards the outlet of the nozzle because

5.38) shows the distribution of

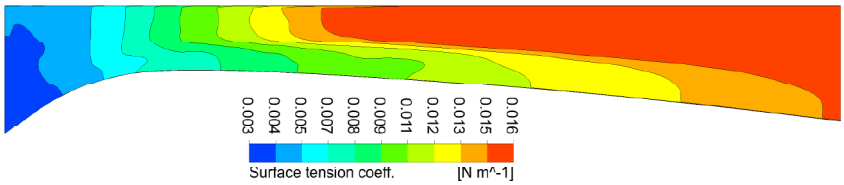

FIGURE 5.37: Surface tension coefficient distribution inside the Gyarmathy nozzle based on the Span-Wagner equation of state.

nucleation rate inside the nozzle. As can be noted from the figure, the nucleation rate is higher in the converging potion of the nozzle but its magnitude is much lower ($\sim 10^{25}$ nucleation per m^3 5.39 5.40)

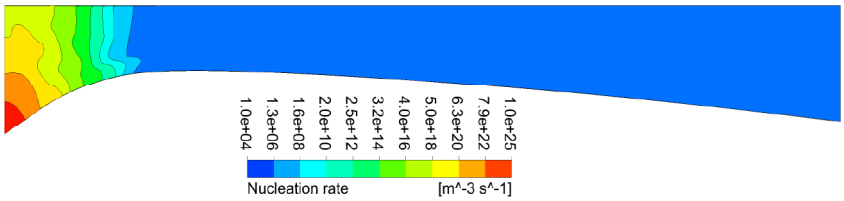

FIGURE 5.38: Nucleation rate distribution inside the Gyarmathy nozzle based on the Span-Wagner equation of state.

respectively show the distribution of droplet number density and droplet diameter inside the nozzle. As can be observed from the figures, the two quantities show opposite behaviour inside the nozzle. The droplet density is higher near the curved wall while the droplet diameter is higher near the flat wall. Also, the droplet diameter is highest near the outlet of the nozzle.

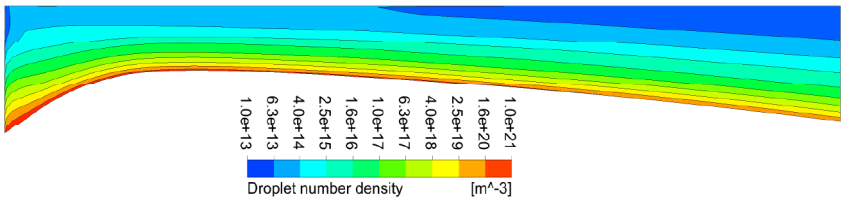

FIGURE 5.39: Droplet number density distribution inside the Gyarmathy nozzle based on the Span-Wagner equation of state.

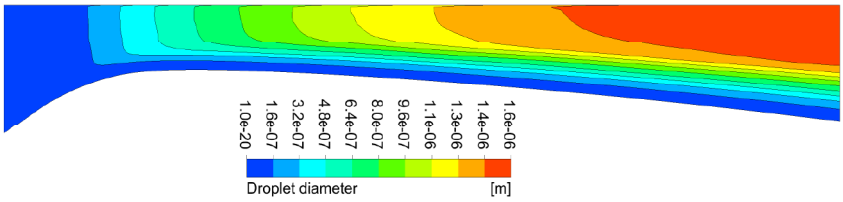

FIGURE 5.40: Droplet diameter distribution inside the Gyarmathy nozzle based on the Span-Wagner equation of state.

5.41) shows the distribution of liquid mass fraction inside the nozzle. A maximum liquid fraction of 0.18 lies near the curved wall at the outlet of the nozzle.

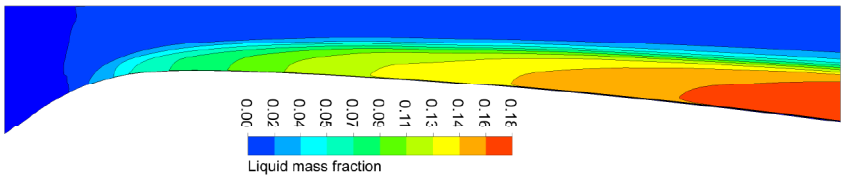

FIGURE 5.41: Liquid mass fraction distribution inside the Gyarmathy nozzle based on the Span-Wagner equation of state.

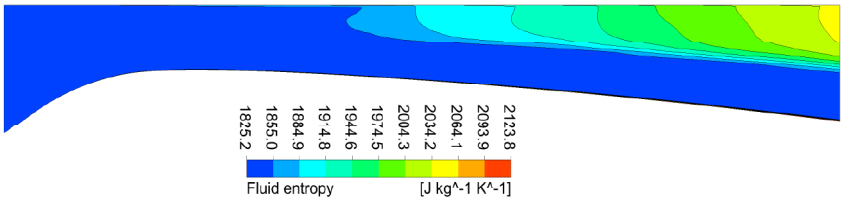

FIGURE 5.42: Fluid entropy distribution inside the Gyarmathy nozzle based on the Span-Wagner equation of state.

5.42) shows the distribution of mixture entropy inside the nozzle. As can be observed, the entropy increases along the flat surface and along downstream of the nozzle. Also, the mixture

5.43

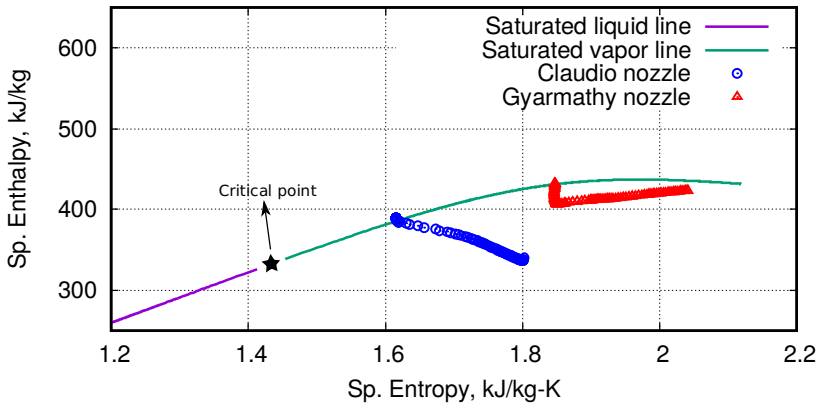

FIGURE 5.43: Nozzle states on an enthalpy–entropy ($h-s$) diagram.

the Claudio Lettieri and Gyarmathy nozzle state points on an enthalpy–entropy diagram. As can be seen from the figure, the nozzle expansion results are physically correct in the sense that the fluid entropy increases along the nozzle downstream direction.

5.4 Guidelines for obtaining converged results from the compressible phase change solvers

Based on the experience gained by us while simulating the phase change process of R-744 inside different converging-diverging nozzles, we conclude that the equilibrium phase change solver

is robust one but can not simulate the flows with non-equilibrium conditions. On the other hand, the droplets based non-equilibrium solver is theoretically more sound, it can simulate non-equilibrium effects but getting correct results from the solver can be a challenge. Here we suggest some guidelines for obtaining converged solutions with compressible phase change solvers in Ansys CFX:

- Before simulating the phase change process, it helps to first obtain a converged, single phase flow field of the vapor based on the boundary conditions for the pressure / mass flow rate. The nucleation model has to be disabled during this step. The single phase solver takes time steps of the order of 10^{-5} second for stable computations and converges easily. The flow field of the supercooled vapor will establish during this step.

- Starting from the initial value, the boundary pressure values can be increased / decreased to the final desired values as a function of either iteration number (if one is using the steady solver) or the time step number (for transient solver). This way one can obtain a converged single phase flow field even for extreme pressure differences across the inlet and outlet of the nozzle.

- One can switch-on the nucleation process in the second step and the phase change process can be simulated at time steps of the order of 10^{-9} second. We observed that both the steady and the transient solvers take similar time steps for stable computations.

- The solvers 'behave well' with thermophysical data from equations of state already available in Ansys CFX like the Redlich-Kwong equation for R-744 and the IAPWS equation for steam. We confirmed this for the flow of both R-744 and water vapor inside different nozzles. The solvers are prone to divergence with thermophysical data in tabular form obtained from some thermophysical property database like NIST Refprop or CoolProp. The solvers also take very low time steps with such thermophysical data. This is due to the spike in thermophysical properties at and around critical point.

- One should check for the extreme values of the thermophysical quantities near the critical point and constrain the respective maximum values to some sensible limits. What maximum value should be allowed at or around critical point is still an unresolved question to us. This is particularly true for the specific heat at constant volume and thermal conductivity etc. which take very high values near the critical point. Plotting the distribution of any physical quantity as a function of pressure and temperature using MATLAB or other package helps in detecting extreme values and Not-a-Numbers (NANs). Such may happen when Refprop routines do not converge near critical point and along saturation lines.

- While importing the thermophysical data from Refprop, one should enable beta properties in Ansys CFX and enable the use of subcooled liquid properties in the material definition. Without this, the solver used to diverge randomly.

- There is an important role played by the maximum allowed critical radius in the domain. Ansys CFX allows values up to 1 mm that means droplets more than 1 mm in size can only grow inside the domain. No phase change is observed under this condition in-spite-of the supercooled vapor in the domain. One can adjust the maximum critical radius allowed in the domain and get a sensible liquid phase distribution in the domain in a way that the fluid mixture entropy increases along the downstream of the nozzle in-spite-of adiabatic boundaries. Too small a critical radius will result in more amount of liquid than that permitted by second law of thermodynamics.

- 121], one can also adjust the empirical constant q_c in order to change the nucleation rate magnitude inside the nozzle. However, the influence of this factor is not investigated in this thesis.

- Better results were observed with structured, hexahedral meshes; the unstructured, tetrahedral meshes induced numerical diffusion. Block structured meshes are recommended where possible.

- Once can use the first order Upwind scheme initially to obtain converged results and then shift to the high resolution schemes for the advection part of the equation. This approach helped to obtain convergence for certain extreme flow situations.

- Lastly, one should have a decent high performance computing machine for simulating the compressible phase change process inside three dimensional geometries of practical importance. With time steps as low as 10^{-10} second and three dimensional complex domains, the simulation process seems to run forever. Our ejector flow simulations with just 543548 hexahedral cells took more than an year to converge on a 28 core machine!

5.5 Summary

The following points summarize the outcomes of the current chapter:

- In this chapter, we used two different compressible phase change solvers available in Ansys CFX for simulating the phase change process of R-744 inside converging-diverging nozzles. The solvers used are the equilibrium phase change solver and the classical nucleation theory based non-equilibrium solver. The aim of the work was partly to gain an understanding about the capability and working of the flow solvers for simulating compressible, high speed phase change problems. We also wanted to validate the setting of various solver parameters. We simulated three different experimental test cases from literature which use supercritical R-744 as the working fluid.

- The equilibrium solver is robust and behaves well with the Refprop based thermophysical data for R-744 in tabular form and gives more accurate results with respect to prediction of pressure distribution in the nozzles.

- The droplets based non-equilibrium solver faces convergence issues with real gas property (RGP) files generated based on NIST Refprop even with time steps as low as 10^{-9} second. 85] equation of state already available in CFX. The extreme values of thermophysical properties near the critical point are responsible for this behaviour. The solver needs thermodynamic data from the metastable states for simulating non-equilibrium conditions which prevail during high speed flows. One should keep this in mind while writing codes for extracting thermophysical data from property databases like Refprop.

- The non-equilibrium solver also requires fine tuning of several 'expert parameters' for obtaining correct results. Converged results could easily be obtained for the flow of R-744 through the Claudio Lettieri nozzle and the Gyarmathy nozzle but the case did not converge for the flow of supercritical R-744 through the Berana nozzle. The reasons could be the nozzle geometry which is very narrow and just one millimeter thick. There is a pressure difference of 55 bar across the nozzle length which is 35 mm. Most importantly, the inlet state is supercritical (90 bar, 318 K) for the nozzle, the critical state occurs somewhere near the throat and extreme variation of thermophysical properties of R-744 near the critical point do not allow convergence.

- Overall, we conclude that Ansys CFX is able to simulate compressible, high speed phase change problems with acceptable accuracy which depends on several factors, among which, the use of real gas property database is the most important one. The experience gained here was used to study the flow of supercritical R-744 inside an ejector geometry, the results for which are given in the next chapter.